Interactions between internal forces, body stiffness, and fluid environment in a neuromechanical model of lamprey swimming

Eric D. Tytell[a,1,2,3], Chia-Yu Hsu[b,2], Thelma L. Williams[c], Avis H. Cohen[a], and Lisa J. Fauci[b]

[a]Institute for Systems Research and Department of Biology, University of Maryland, College Park, MD; [b]Department of Mathematics and Center for Computational Science, Tulane University, New Orleans, LA; and [c]Department of Mechanical and Aerospace Engineering, Princeton University, Princeton, NJ

Edited* by Charles S. Peskin, New York University, and approved September 6, 2010 (received for review August 5, 2010)

Animal movements result from a complex balance of many different forces. Muscles produce force to move the body; the body has inertial, elastic, and damping properties that may aid or oppose the muscle force; and the environment produces reaction forces back on the body. The actual motion is an emergent property of these interactions. To examine the roles of body stiffness, muscle activation, and fluid environment for swimming animals, a computational model of a lamprey was developed. The model uses an immersed boundary framework that fully couples the Navier–Stokes equations of fluid dynamics with an actuated, elastic body model. This is the first model at a Reynolds number appropriate for a swimming fish that captures the complete fluid-structure interaction, in which the body deforms according to both internal muscular forces and external fluid forces. Results indicate that identical muscle activation patterns can produce different kinematics depending on body stiffness, and the optimal value of stiffness for maximum acceleration is different from that for maximum steady swimming speed. Additionally, negative muscle work, observed in many fishes, emerges at higher tail beat frequencies without sensory input and may contribute to energy efficiency. Swimming fishes that can tune their body stiffness by appropriately timed muscle contractions may therefore be able to optimize the passive dynamics of their bodies to maximize peak acceleration or swimming speed.

computational fluid dynamics | elasticity | locomotion

The mechanics of fish swimming is a complex problem. The bodies of fishes are elastic structures that deform in response to fluid forces but also affect the fluid moving around them. Much progress has been made in recent years understanding the fluid motion around swimming fishes (1), along with the nonlinear properties of muscle (2) and the elastic behavior of fish bodies (3, 4). Computational fluid dynamics (CFD) has also become increasingly feasible as a tool for studying fish swimming, but in most cases, the body motion, even for flexible animals, is prescribed (for examples, see refs. 5–8).

However, all of these previous studies examined body mechanics separately from fluid mechanics. No work has yet solved the coupled fluid-structure interaction (FSI) problem for fish swimming: the transformation from muscle activation to fluid and body motion at high Reynolds number. The relative contributions of inertial and viscous forces is described by the Reynolds number $Re = \rho UL/\mu$, where ρ and μ are the fluid's density and viscosity, respectively, and U and L are the fish's swimming speed and body length. At high but noninfinite Re, inertial forces dominate, but viscous interactions cannot be neglected entirely because they are critical for vortex shedding sharp edges like fish fins (9).

Several recent CFD models of fishes have included some FSI, coupling center-of-mass motion to fluid dynamic forces with otherwise prescribed body kinematics (e.g., 5, 6). Other studies (10, 11) have used simplified fluid models to study fully coupled models for fish swimming. Still others (12, 13) used an inverse approach: They start with the measured kinematics, then estimate the hydrodynamic forces on the body and then the muscle forces required to generate the prescribed kinematics.

The model presented here includes an actuated, viscoelastic body, based on that of a lamprey swimming in a 2D fluid domain. We use an immersed boundary framework (14) with an adaptive, parallel implementation developed by Griffith (15). The motion of the body emerges as a balance between internal muscular force and external fluid forces. Depending on external parameters such as viscosity and internal parameters such as body stiffness, the swimmer can achieve different levels of performance, including rapid acceleration or high steady speed.

Additionally, we examine muscle activity and body bending. We include a simple model of muscle force development (after ref. 11). In most fishes, the phase difference between muscle activation and body bending increases from head to tail (16, 17). As a consequence, muscles near the tail may be active during lengthening, absorbing energy. Muscles produce energy (positive work) when they generate force while shortening, but they absorb energy (negative work) when they generate force, but not enough to resist being lengthened by an external force. Negative muscular work near the tail is not necessarily inefficient for propulsion, because it stiffens the tail against the fluid, allowing more anterior muscles to transfer positive work through the tail to the fluid (18). We consider the conditions under which this neuromechanical phase lag can develop in the absence of sensory inputs.

Results

Simulations were performed with different values for body and fluid properties. Table 1 shows simulation parameters and results of all computations. Also included is a comparison to data from eels (3, 19, 20), a fish with a similar swimming mode as lampreys. In all figures below, simulation 1 is used as a reference and is shown in black.

Fig. 1 shows fluid motion around the swimmer during steady swimming (see also Movie S1). A single strong vortex is shed each time the tail reverses direction. Multiple weak secondary vortices are also produced. This reference swimmer, with an activation frequency of 1 Hz, accelerates from rest to a steady-state speed of 0.50 $L{\cdot}s^{-1}$ (Fig. 2*A*). Fluid stresses were calculated according to the method of Williams et al. (21) (see *Materials and Methods*

Author contributions: E.D.T., T.L.W., A.H.C., and L.J.F. designed research; C.-Y.H. performed research; E.D.T. and C.-Y.H. analyzed data; and E.D.T., T.L.W., and L.J.F. wrote the paper.

The authors declare no conflict of interest.

*This Direct Submission article had a prearranged editor.

[1]To whom correspondence should be addressed. E-mail: tytell@jhu.edu.

[2]E.D.T. and C.-Y. H. contributed equally to this work.

[3]Present address: Department of Mechanical Engineering, The Johns Hopkins University, 112 Hackerman Hall, 3400 North Charles Street, Baltimore, MD 21218.

This article contains supporting information online at www.pnas.org/lookup/suppl/doi:10.1073/pnas.1011564107/-/DCSupplemental.

Table 1. Simulation parameters and computed values

		Eel*	Reference	Viscosity		Stiffness			Stiffness + muscle force		Frequency	
Parameters	simulation number		1	2	3	4	5	6	7	8	9	10
	dynamic viscosity μ (mPa·s)	1	1	0.5	10	1	1	1	1	1	1	1
	Young's modulus E (MPa)	0.39	0.76	0.76	0.76	0.60	0.66	1.31	0.64	0.98	0.76	0.76
	muscle force scale factor		1	1	1	1	1	1	0.5	2	1	1
	activation frequency f (Hz)	1.48	1	1	1	1	1	1	1	1	0.5	1.5
Computed results	tail beat amplitude A (L)	0.07	0.16	0.16	0.13	0.24	0.21	0.08	0.12	0.16	0.20	0.10
	swiming speed U ($L{\cdot}s^{-1}$)	0.53	0.50	0.52	0.25	0.22	0.36	0.37	0.44	0.53	0.23	0.64
	inital acceleration ($L{\cdot}s^{-2}$)		0.30	0.32	0.16	0.30	0.31	0.12	0.14	0.48	0.12	0.20
	wave speed V ($L{\cdot}s^{-1}$)	0.89	0.69	0.73	0.57	0.77	0.70	0.67	0.59	0.77	0.41	0.87
	act. wave speed V_{act} ($L{\cdot}s^{-1}$)	1.55	0.88	0.86	0.88	0.88	0.88	0.88	0.88	0.88	0.44	1.32
	wave speed/act. speed V/V_{act}	0.58	0.78	0.84	0.65	0.87	0.79	0.76	0.67	0.87	0.94	0.66
	St	0.37	0.62	0.63	1.03	2.13	1.15	0.41	0.53	0.62	0.86	0.46
	muscle power coef. $C_{P,mus}$		0.122	0.094	1.119	3.033	0.491	0.100	0.105	0.129	1.270	0.029

*Values estimated from data published in refs. 3, 19, 20.

below). The integral of fluid stress in the swimming (axial) direction over the entire body fluctuates over time but integrates to zero over a tail beat period (Fig. 2*A*). These fluctuations in force and speed are due to the cyclic changes in body shape.

Impulse I_i was calculated by integrating the stress tensor σ on 10 regions along the body over a cycle period T: $\int_t^{t+T}\int_{\Sigma_i}\mathbf{a}\cdot\sigma\cdot\mathbf{n}\,ds\,dt$, where Σ_i is the ith region of the body, and $\mathbf{a}$ and $\mathbf{n}$ are vectors in the axial direction and normal to the body surface. Impulse is positive along most of the body (thick line in Fig. 2*B*) except near the head. The tail tip also produces net drag because of the spatial discretization. The forces applied by the immersed boundary, even at high grid resolution, are regularized so that the tail tip, in effect, does not end in a sharp point. Fluid separates around the slightly blunt tip, resulting in drag. The force regularization also limits the flexibility of the thinnest portion of the tail region, which results in the fluctuation in curvature and impulse along the body (Fig. 2*B*). Performance is not affected by these fluctuations (see *Materials and Methods* below). Tangential forces (filled gray bars), which are primarily due to skin friction, always contribute negatively, while normal forces (open bars), primarily an effect of pressure, are mostly positive.

2D CFD Force Calculations Match the Reactive Model Better Than the Resistive Model. Fluid forces as computed from the Navier–Stokes solutions were compared to two analytical models: Lighthill's elongated body theory, based on reactive forces (22), and Taylor's resistive theory (11, 23). As inputs to the two analytical models, we use the kinematics as derived from CFD and the instantaneous speed U of the center of mass.

Forces cannot be compared directly because the analytical models produce estimates of force on a three-dimensional body, while the current 2D CFD model produces a force per unit height. Nevertheless, the shapes of the curves are informative. Fig. 3 shows the estimates of lateral forces over three tail beat cycles. Peaks in the CFD estimate (in $mN{\cdot}cm^{-1}$; circles, left axis) correspond to vortex shedding (arrows). Forces from the reactive model (in mN; dashed line, right axis) match the shape of the curve from CFD well, including the shape of the peaks. Dividing the reactive force estimate by the CFD calculations results in a scale factor of 0.29 cm, equal to the average width of the body. The resistive force estimates (dotted line, right axis) are approximately 90° out of phase with the CFD values.

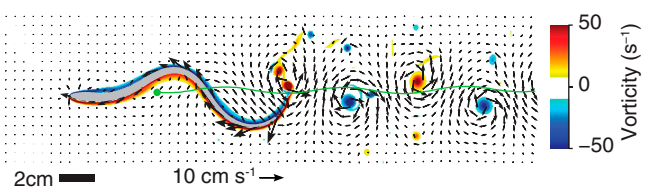

Fig. 1. Example flow patterns around the reference swimmer (shown in gray). Arrows indicate flow velocity; background color shows vorticity. The green line indicates the path of the center of mass.

Swimming Kinematics Are an Emergent Phenomenon. To examine how the swimming movements emerge as a result of the fluid-structure interaction, the viscosity was varied (Table 1, simulations 2 and 3). All other activation parameters and mechanical properties of the body remained the same. Fig. 4*A* shows outlines of the swimmer in different viscosities. The curvature wavelength (Fig. 4*B*) changes with fluid viscosity (see also Movie S2), even though the activation wavelength is identical.

There Is an Optimal Body Stiffness for Maximum Steady Speed or for Maximum Acceleration. Swimmers with Young's modulus ranging from 0.60 MPa to 1.31 MPa were simulated (Table 1, simulations 4–6). The muscle activation parameters were kept constant. Fig. 5 *A* and *B* show swimming speed and outlines of the four swimmers. We compared the mean acceleration sustained during the first tail beat and mean steady swimming speed. A local optimal stiffness for maximum sustained acceleration is near 0.66 MPa (green bar, Fig. 5*C*). The floppiest swimmer (tan line, Fig. 5*A*) initially accelerates fastest but does not maintain acceleration after the first half cycle. An optimum stiffness for maximum sustained swimming speed is higher than that for acceleration (Fig. 5*D*) and is located near 0.76 MPa. Finally, muscle power was calculated. The muscle power coefficient $C_{P,mus}$ normalizes

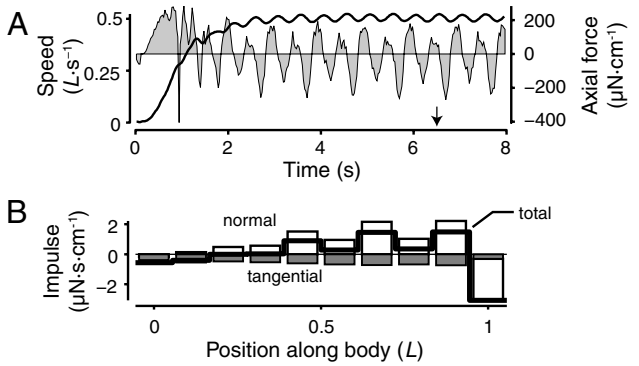

Fig. 2. The swimmer reaches a steady speed and produces net positive axial impulse along most of its body. (*A*) Swimming speed (solid line, left axis) and force per unit height in the axial direction (gray regions, right axis). Arrow indicates the time of Fig. 1. (*B*) Axial impulse per unit height produced over a cycle period during steady swimming. Impulse values due to normal and tangential stresses are in open and filled gray bars, respectively. Net axial impulse per unit height is shown with a thick line.

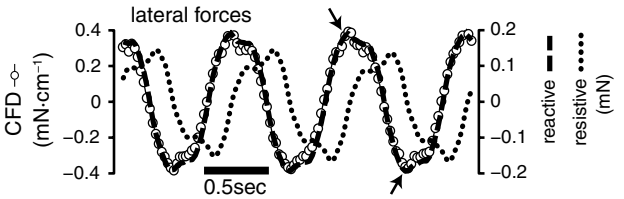

Fig. 3. Comparison of fluid forces as calculated from analytical models and the CFD model. The plot shows time course of lateral forces from the Navier–Stokes solution (left axis, open symbols), Lighthill's large amplitude elongated body theory (right axis, "reactive," dashed line) (22), and Taylor's resistive model (right axis, "resistive," dotted line) (11, 23). Arrows indicate two peaks due to vortex shedding.

muscle power according to the swimming speed (see *Materials and Methods* below). The stiffest swimmer, although slower than the reference, has the smallest power coefficient (Fig. 5*E*).

When peak muscle forces are kept constant, swimmers with extremely low or high stiffness cannot move effectively (Fig. 5). Therefore, two other swimmers were simulated: one with low body stiffness and weak muscles that produce half the peak force as those in the reference, and another with high body stiffness and muscles that are twice as strong (Table 1, simulations 7 and 8). These two swimmers reached nearly the same steady swimming speed as the reference (0.44 and 0.53 $L{\cdot}s^{-1}$ vs. 0.50 $L{\cdot}s^{-1}$). Tail amplitude was lower for the floppy, weak swimmer (0.12*L*) and higher for the stiff, strong one (0.16*L*), the opposite of the result when stiffness was changed without altering muscle force. The stiff model with strong muscles accelerated the fastest of any simulation, about 60% faster than the reference simulation, yet its power coefficient was close to that of the reference (0.129 vs. 0.122). The floppy model with weak muscles accelerated slowly, but required relatively little power (Table 1).

Negative Work Is Produced Near the Tail When Muscle Forces Are Low Relative to Fluid Forces. The mechanical parameters involved in the production of a neuromechanical phase lag between activation and curvature (16) were examined. A lag was observed in three simulations: 1.5 Hz activation frequency (simulation 10, Table 1), a floppy body with weak muscles (simulation 7), and in high viscosity fluid (simulation 3). Fig. 6*A* shows the relative phase of activation and curvature for these simulations and the reference. The phase lag increases so much that caudal muscles (the last 20% of the body) were active during lengthening, producing negative work. These three simulations were similar to each other and different from the others because they had low average muscle forces compared to average fluid forces (Fig. 6*B*). The low muscle forces arise for different reasons. For the 1.5 Hz swimmer, the fractional time for muscle force development was the same as for the reference, but the cycle period was shorter, so that muscle force never reached its peak value. For the floppy body, weak muscle case, the peak muscle force was halved as part of the initial simulation parameters. For the high viscosity case, the muscle force remained the same, but the fluid forces went up, largely due to the increased skin friction in high viscosity fluid.

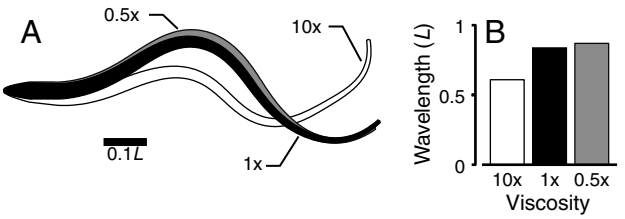

Fig. 4. Identical swimmers in fluids of different viscosity have different kinematics. (*A*) Outlines of swimmers in three viscosities (gray, 0.5×; black, 1×; and white, 10×water) at the same time. (*B*) Body wavelength in fluid of different viscosities. Activation wavelength is identical.

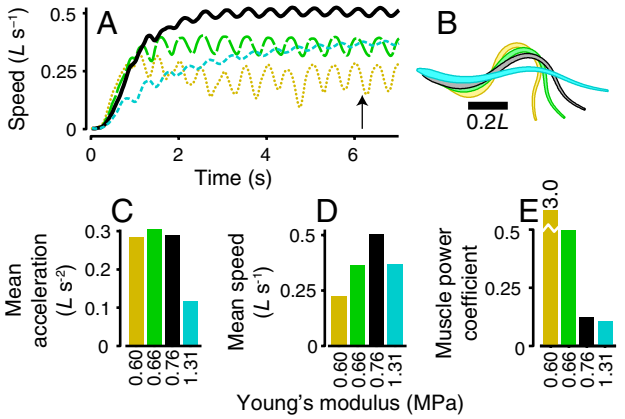

Fig. 5. For a given muscle activation pattern, there are different optimal stiffness values for maximum acceleration or steady swimming speed. The plots show four swimmers with increasing stiffness: tan dotted line, simulation 4, Table 1; green long dashes, simulation 5; black, reference simulation; and cyan short dashes, simulation 6. (*A*) Swimming speed vs. time. (*B*) Body outlines for each swimmer at the time indicated by the arrow on panel *A*. (*C*) Mean acceleration during the first tail beat. (*D*) Mean steady swimming speed. (*E*) Muscle power coefficient $C_{P,\mathrm{mus}}$.

Discussion

To the authors' knowledge, this study represents a unique numerical model of undulatory locomotion that accurately simulates the fluid-structure interaction, fully coupling internal muscle mechanics and an elastic body to an incompressible, viscous fluid governed by the Navier–Stokes equations at realistically high Reynolds numbers. Researchers as early as Sir James Gray in 1933 have remarked on the importance of solving the FSI problem for animal locomotion (7, 18, 24, 26). FSI problems at low *Re* have been more tractable (e.g., refs. 27, 28). Using an adaptive Navier–Stokes solver (15), our swimmer achieves a Reynolds number of order 10^4 based on body length and swimming speed, comparable to that of swimming eels and lampreys (17, 19). At these high values of *Re*, other studies with Navier–Stokes fluid solvers have coupled the motion of the center of mass to the fluid (e.g., refs. 5, 6) or linked one or two elastic joints to the fluid (29, 30). Other models with FSI prescribe some aspects of wave kinematics or use simplifications of the equations of fluid motion (10, 11, 13, 31–33).

Our results suggest that one common simplification, the forces due to Taylor's resistive model (23) used by McMillen et al. (11) and by Ekeberg (33) do not have the correct phase relative to the

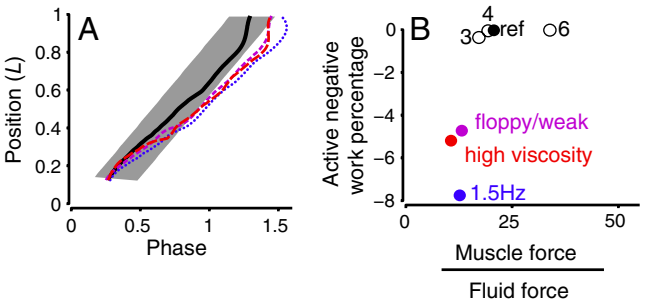

Fig. 6. A phase lag between muscle activation and curvature corresponds to negative muscle work near the tail and is produced when muscle forces are low compared to fluid forces. (*A*) Phase of curvature and muscle activation along the body. Gray bar shows the activated muscle region, while lines show the position of zero curvature (black solid line, reference; dark blue dots, 1.5 Hz; purple short dashes, floppy body with weak muscles; red long dashes, high viscosity). (*B*) Negative muscle work produced in the last 20% of the body as a fraction of the total muscle work, plotted against rms muscle force divided by rms fluid forces in the lateral direction. Numbers indicate simulation number, Table 1.

CFD estimates (Fig. 3). In the resistive model, flow around one segment of the body is assumed not to affect flow around any other segment. This assumption is clearly violated, because flow moves along the body (see *SI* movies). Each segment is also assumed to be equivalent, while our results (Figs. 1 and 2*B*) and Lighthill's elongated body theory (22) suggest that vortex shedding at the tail tip is particularly important for determining the timing of total force on the body. However, the quality of the agreement between CFD and elongated body theory may have been elevated by the 2D CFD computations. In 2D, vortices can only be shed at the tail tip, as required by Lighthill's approximation (22). Future calculations in 3D will allow vortex shedding along the dorsal and ventral surfaces. In fishes, such vortices represent a large fraction of the total vorticity (34). This additional vortex shedding may affect the quality of the agreement with elongated body theory.

The balance between such fluid forces and the internal muscle and spring forces determines the motion of the body. Both the kinematics and the swimming performance are an emergent property of the simulation. Figs. 4 and 6 show that identical swimmers produce shorter curvature wavelengths, which correspond to a larger neuromechanical phase shift, when placed in high viscosity fluid. A similar effect was observed in lungfish (*Protopterus annectens*) swimming in high viscosity fluid (35) .

Kinematics and performance are also strongly affected by internal parameters, particularly body stiffness. For a given set of activation parameters, there are different optimum values of stiffness for rapid acceleration or high steady speed (Fig. 5). Due to the computational cost of the simulations, the stiffness parameters are spaced widely. Nevertheless, our results demonstrate the existence of a stiffness value that optimizes acceleration and a different value that optimizes swimming speed. Relatively stiff models reach the highest swimming speed, while floppier models accelerate most rapidly. By contrast, in living fishes, stiff-bodied fishes generally have the highest accelerations. For instance, both barracudas (*Sphyraena*) and lampreys are elongate fishes, but barracudas accelerate faster and have much stiffer bodies (36). These biological observations do not contradict our computational results, because we varied stiffness while keeping all other muscle and activation parameters constant, while it is unlikely that the muscles and activation pattern are identical for barracudas and lampreys. For example, barracudas may have a higher physiological cross-sectional area of muscle, which corresponds to higher muscle force. Supporting this idea, the highest accelerations in our simulations are seen when muscle force and body stiffness are increased together (simulation 8, Table 1).

Swimming speed was also strongly dependent on the activation frequency. In all cases, the muscles' twitch dynamics were kept constant. From 0.5 to 1.5 Hz, swimming speed was approximately proportional to activation frequency (simulations 1, 9, and 10, Table 1), even though the body amplitude decreased by a factor of two. The decrease in amplitude is surprising, because kinematic data from swimming fishes generally shows a positive correlation between amplitude and swimming speed (19). However, swimming fishes also recruit additional motor units and fast twitch white fibers as activation frequency increases (25), features that are not present in our simulations. Nevertheless, it is instructive to examine the differences between the 1.5 Hz swimmer and the others.

In particular, the high swimming speed and low amplitude of the 1.5 Hz swimmer suggests that it generates thrust more effectively than the other swimmers. This may be a consequence of the negative muscular work produced near the tail due to the large phase lag between muscle activation and tail motion (Fig. 6). This phase lag helps to determine the angle of the tail as it moves, which is critical for thrust development (22). Supporting this idea, the 1.5 Hz swimmer also produces a different wake than the other swimmers (see Movie S3).

Simulations at high viscosity or with a floppy body and weak muscles also developed a phase lag. We suggest that the neuromechanical lag arises when average muscle forces are low relative to fluid forces (Fig. 6*B*). This hypothesis may also explain the results from McMillen et al. (11), who found small phase lags in two swimmers: (*i*) with no taper, and (*ii*) with no damping. According to the current hypothesis, these swimmers should have relatively high muscle forces. First, without taper, the mechanical advantage of the muscles near the tail is higher, whereas the fluid forces remain roughly the same. Second, without damping, the relative muscle force should also be higher. The damping term in (11) produces an internal force that resists changes in curvature, while muscular force acts to change curvature. Thus, internal damping opposes the muscles, reducing the effective muscle force. Without damping, the muscle force that can be applied to the fluid is higher.

Although our model is two-dimensional, the results are comparable to those from swimming fishes. The simulated lamprey had a stiffness comparable to that of an eel (Table 1) (3). At 1.5 Hz activation frequency, the simulation matches data from eels quite well: within 15% for most parameters (Table 1). Simulation parameters were not optimized to match the eel. Simulations were compared to eels and not lampreys, because lamprey data (17) are not available for such a low swimming speed. Indeed, it should be noted that eels rarely swim slower than 0.5 $L{\cdot}s^{-1}$ (19), whereas the fastest swimmer in this study only reached a maximum speed of 0.6 $L{\cdot}s^{-1}$. Swimming speeds are relatively low, most likely because the muscle model parameters remained constant as activation frequency increased. Real fishes, in contrast, recruit additional muscle and faster fibers at high activation frequencies (25).

In addition, other model predictions are different from in vivo data with respect to activation frequency. The model predicts that curvature wavelength and neuromechanical phase lag (Fig. 6) depend strongly on activation frequency (Table 1). In contrast, results from swimming fishes indicate these parameters remain fairly constant across frequencies (16, 17, 19). Again, increased muscle recruitment (25) at high frequencies may explain the differences, or sensory feedback may be necessary to maintain the neuromechanical phase lag as activation frequency changes.

Finally, our results indicate that swimming performance is quite sensitive to mechanical parameters. The local optimal stiffness for maximum acceleration is approximately 15% smaller than an optimum for maximum swimming speed. This has two implications. First, neurophysiologists must be cautious in interpreting data from motor neurons. The model suggests that identical motor outputs can produce substantially different performance if the biomechanical parameters are even slightly different. Second, fishes may be able to take advantage of this sensitivity to biomechanics. Stiffness of the body, for example, can be increased by 200% or more by appropriately timed muscle activation (3). Peak muscle force can also be tuned by recruiting different numbers of motor units. Fishes may therefore be able to tune the passive dynamics of their bodies to maximize peak acceleration or swimming speed.

In summary, we have shown, first, that passive mechanical properties, particularly stiffness, are crucial for effective swimming. Second, sensory feedback is not required for high performance, provided the mechanical parameters are tuned appropriately. Finally, swimming performance appears to be quite sensitive to the mechanical parameters; small changes in stiffness can result in large changes in performance.

Future work will extend the current model to 3D so that we can examine the role of body shape. The 3D model will produce vorticity along its length, as has been observed experimentally (34), which will change the distribution of forces along the body. Simulations with different body shapes will shed vortices differ-

ently along their lengths, ultimately resulting in different swimming kinematics and performance.

We will also examine the role of sensory feedback. We have shown that feedback is not necessary for stable, effective swimming in still water. Future work will use controlled perturbations to investigate the relative importance of passive mechanical stability of the swimmer and stability mediated by sensory feedback. For example, the current swimmer is neutrally stable in yaw (*SI* movies; see also ref. 33); sensory feedback is therefore required to maintain a heading. Passive stability is likely to be particularly important in the 3D model, which will need stability in pitch and roll. We will therefore incorporate models of the CPG circuit (after ref. 37) and proprioceptive sensory cells (38), then perturb the model with realistic flows, such as cross flows, vortex rings, and shear layers.

Materials and Methods

The immersed boundary method (14) provides a framework for coupling elastic dynamics of flexible boundaries with a viscous, incompressible fluid. These elastic objects are accounted for by suitable contributions to a force term in the incompressible Navier–Stokes equations. The force of the object on the fluid is a Dirac delta-function layer of force supported only by the region of fluid that coincides with material points of the object. Once these forces on the fluid are accounted for, the fluid dynamics equations are solved on a regular, finite difference grid. At each time step, the no-slip condition at the immersed boundary is enforced by moving its material points at the updated and interpolated fluid velocity. To capture boundary layers and vortex shedding at high Reynolds numbers, an adaptive, parallel implementation of the immersed boundary method was used (15). Because of computational limitations, simulations are performed on a 2D grid.

The computational lamprey, whose length is $L = 12.6$ cm, is immersed in a fluid domain that is five body lengths wide and three body widths high (252 cm × 37.8 cm). Boundary conditions are no-slip on the top and bottom and no-penetration on the sides. The adaptive immersed boundary method (15) uses three levels of grid refinement: Regions that contain immersed boundary points and/or vorticity above a threshold are discretized at the highest refinement level ($\Delta x = 0.025$ cm), whereas most of the domain is discretized at the coarsest level ($\Delta x = 0.4$ cm). Computations were performed using a base time step of $\Delta t = 0.25 \times 10^{-4}$ s. Convergence studies were conducted at half and twice the smallest grid refinement. Results from the finest resolutions are nearly indistinguishable from the current results. For example, mean swimming speed changes by less than 2%. In addition, computations were tested with larger fluid domains to ensure that the size of the tank had little or no influence on the simulations.

Body Model. Our simulated lamprey is built out of three segmented filaments: a stiff center line with 640 links and two lateral sides, each with 320 links (Fig. S1). The structure of the body was chosen to reproduce, abstractly, the geometry and mechanical properties of fish bodies. The links along the center filament and the crosslinks that connect the center line to the lateral sides are modeled as passive, Hookean springs with stiffness constant S_1. The links along the lateral sides are modeled as springs with stiffness constant S_2, but they do not resist compression (similar to collagen fibers). The links along the lateral sides also support active muscle contractions (Fig. S1*C*) that are based upon the kinetic model of lamprey muscle dynamics presented in ref. 11. For simplicity, we do not include the nonlinear dependence of muscle force on length or velocity. The body inherits damping properties from the viscous fluid in which it is immersed.

The activation pattern was modeled on that of eels and lampreys (17, 19, 20). Undulatory muscle force is produced in the posterior 88% of the body, representing the region caudal to the gills in the lamprey. Of the segments on either side of the body, 30% are active at any given time, and these activated regions progress down the body with an activation wave speed V_{act} of 0.88 L·cycle^{-1}, so that one full activation wave is present on the body (Fig. S1*A*). To model a free swimmer, the immersed boundary framework requires that all internal muscle and spring forces sum to zero at every point in time (14).

The macroscopic bending modulus was estimated using the procedure in ref. 39. The body was bent at a constant curvature κ and the total potential energy E_κ stored in all of the springs was calculated. For a homogenous elastic beam, the stored energy is related to curvature by $E_\kappa = \frac{1}{2}EI\kappa^2 L$, where EI is the flexural stiffness, composed of the Young's modulus E and the second moment of area I. Because the model is 2D, the units of EI estimated through this procedure are N·m. To estimate an approximate 3D equivalent, we multiply by the average diameter of the body (0.29 cm). Similarly, the second moment of area I of the cross-section was approximated by that of a circle with diameter 0.29 cm.

Postprocessing. The center of mass of the body was determined by integrating position across the area of the swimmer, assuming constant density. Mean center of mass speed U is calculated during steady swimming, when the fluctuations in speed are less than 5%. Initial acceleration is the mean of dU/dt during the first cycle period. Body curvature κ is approximated numerically using a quintic smoothing spline (19).

Kinematic variables including amplitude, wave speed, and wavelength were determined according to the method described in detail in ref. 19 by tracking zero crossings in curvature (circles in Fig. S1). Amplitude A is half the maximum lateral excursion at the tail tip. Wave speed V is estimated by a linear fit of the position of a zero in curvature over time, while wave length is twice the arc length between successive zeros in curvature. Strouhal number St is $2fA/U$, where f is the activation frequency. The ratio of the curvature wave speed V to activation wave speed V_{act} is a measure of the neuromechanical phase lag (11); when V/V_{act} is less than one, the phase lag between curvature and activation increases along the body.

The rate of muscle work per unit height P^i in a segment i is $f^i_{mus}(dl^i/dt)$ where f^i_{mus} is the muscle force in that segment and l^i is its instantaneous length. Average muscle power $\bar{P}$ per cycle was determined by summing over all points, integrating over a cycle period, and dividing by the cycle duration. For a 2D swimmer, the power P_0 required to overcome drag at a steady forward speed U should scale as $P_0 = \frac{1}{2}\rho c U^3$, where c is the perimeter of the swimmer (19). The muscle power coefficient $C_{P,mus} = \bar{P}/P_0$ thus provides a way to compare the relative muscle power required to travel at a steady speed, even when the speeds are different.

The jump in the fluid stress tensor across the boundary was calculated according to the method in ref. 21. The fluid stress tensor σ is $-p\mathbf{I} + \mu(\nabla\mathbf{u} + (\nabla\mathbf{u})^T)$, where p and $\mathbf{u}$ are the fluid pressure and velocity, respectively, and $\mathbf{I}$ is the identity tensor. To approximate this value numerically, the fluid velocity $\mathbf{u}$ and the pressure p are interpolated from the Eulerian finite difference fluid grid onto a Lagrangian coordinate system defined by the normal and tangential vectors of the body's boundary. In the interpolation, we are careful to use grid points outside of the boundary (21). Gradients are evaluated using a second-order central difference algorithm. Fluid forces were also estimated analytically according to reactive force theory (22) and resistive force theory as expressed in ref. 11.

ACKNOWLEDGMENTS. This work was supported by the National Institutes of Health National Research Service Award Grant F32 NS054367 (to E.D.T.) and a Collaborative Research in Computational Neuroscience Grant R01 NS054271 (to A.H.C.). L.J.F. and C.-Y.H. were also supported by National Science Foundation Grant DMS-0652795 (to L.J.F.).

1. Lauder GV, Tytell ED (2006) *Fish Biomechanics*, eds RE Shadwick and GV Lauder (Academic, San Diego), pp 425–468.
2. Williams TL (2010) A new model for force generation by skeletal muscle, incorporating work-dependent deactivation. *J Exp Biol* 213:643–650.
3. Long JH (1998) Muscles, elastic energy, and the dynamics of body stiffness in swimming eels. *Am Zool* 38:771–792.
4. Long JH, Adcock B, Root RG (2002) Force transmission via axial tendons in undulating fish: A dynamic analysis. *Comp Biochem Phys A* 133:911–929.
5. Borazjani I, Sotiropoulos F (2010) On the role of form and kinematics on the hydrodynamics of self-propelled body/caudal fin swimming. *J Exp Biol* 213:89–107.
6. Kern S, Koumoutsakos P (2006) Simulations of optimized anguilliform swimming. *J Exp Biol* 209:4841–4857.
7. Mittal R (2004) Computational modeling in biohydrodynamics: Trends, challenges, and recent advances. *IEEE J Oceanic Eng* 29:595–604.
8. Dong H, Bozkurttas M, Mittal R, Madden PGA, Lauder GV (2010) Computational modelling and analysis of the hydrodynamics of a highly deformable fish pectoral fin. *J Fluid Mech* 645:345–373.
9. Batchelor GK (1973) *An introduction to fluid dynamics* (Cambridge Univ Press, Cambridge).
10. Bowtell G, Williams TL (1991) Anguilliform body dynamics—modeling the interaction between muscle activation and body curvature. *Philos T R Soc Lon B* 334:385–390.
11. McMillen T, Williams T, Holmes P (2008) Nonlinear muscles, passive viscoelasticity and body taper conspire to create neuromechanical phase lags in anguilliform swimmers. *PLoS Comput Biol* 4:e1000157.
12. Pedley TJ, Hill SJ (1999) Large-amplitude undulatory fish swimming: Fluid mechanics coupled to internal mechanics. *J Exp Biol* 202:3431–3438.
13. Cheng JY, Pedley TJ, Altringham JD (1998) A continuous dynamic beam model for swimming fish. *Philos T R Soc Lon B* 353:981–997.

14. Peskin CS (2002) The immersed boundary method. *Acta Numer* 11:479.
15. Griffith BE, Hornung RD, McQueen DM, Peskin CS (2007) An adaptive, formally second order accurate version of the immersed boundary method. *J Comput Phys* 223:10–49.
16. Wardle CS, Videler JJ, Altringham JD (1995) Tuning in to fish swimming waves: Body form, swimming mode and muscle function. *J Exp Biol* 198:1629–1636.
17. Williams TL, et al. (1989) Locomotion in lamprey and trout: The relative timing of activation and movement. *J Exp Biol* 143:559–566.
18. Blight AR (1977) The muscular control of vertebrate swimming movements. *Biol Rev* 52:181–218.
19. Tytell ED (2004) The hydrodynamics of eel swimming. II. Effect of swimming speed. *J Exp Biol* 207:3265–3279.
20. Gillis GB (1998) Neuromuscular control of anguilliform locomotion: Patterns of red and white muscle activity during swimming in the american eel *Anguilla rostrata*. *J Exp Biol* 201:3245–3256.
21. Williams HAR, Fauci LJ, Gaver DP (2009) Evaluation of interfacial fluid dynamical stresses using the immersed boundary method. *Discret Cont Dyn S-B* 11:519–540.
22. Lighthill J (1971) Large-amplitude elongated-body theory of fish locomotion. *P Roy Soc Lond B Bio* 179:125–138.
23. Taylor GI (1952) Analysis of the swimming of long and narrow animals. *P Roy Soc Lond A Mat* 214:158–183.
24. Gray J (1933) Studies in animal locomotion. I. The movement of fish with special reference to the eel. *J Exp Biol* 10:88–104.
25. Jayne BC, Lauder GV (1994) How swimming fish use slow and fast muscle fibers: Implications for models of vertebrate muscle recruitment. *J Comp Physiol A* 175:123–131.
26. Jordan CE (1996) Coupling internal and external mechanics to predict swimming behavior: A general approach? *Am Zool* 36:710–722.
27. Dillon RH, Fauci LJ, Omoto C, Yang X (2007) Fluid dynamic models of flagellar and ciliary beating. *Ann NY Acad Sci* 1101:494–505.
28. Visbal M, Gordnier R, Galbraith M (2009) High-fidelity simulations of moving and flexible airfoils at low reynolds numbers. *Exp Fluids* 46:903–922.
29. Vanella M, Fitzgerald T, Preidikman S, Balaras E, Balachandran B (2009) Influence of flexibility on the aerodynamic performance of a hovering wing. *J Exp Biol* 212:95–105.
30. Toomey J, Eldredge JD (2008) Numerical and experimental study of the fluid dynamics of a flapping wing with low order flexibility. *Phys Fluids* 20:073603–10.
31. Alben S (2010) Passive and active bodies in vortex-street wakes. *J Fluid Mech* 642:95–125.
32. Shoele K, Zhu Q (2009) Fluid-structure interactions of skeleton-reinforced fins: Performance analysis of a paired fin in lift-based propulsion. *J Exp Biol* 212:2679–2690.
33. Ekeberg Ö, Grillner S (1999) Simulations of neuromuscular control in lamprey swimming. *Phil T R Soc Lond B* 354:895–902.
34. Tytell ED (2006) Median fin function in bluegill sunfish, *Lepomis macrochirus*: Streamwise vortex structure during steady swimming. *J Exp Biol* 209:1516–1534.
35. Horner AM, Jayne BC (2008) The effects of viscosity on the axial motor pattern and kinematics of the african lungfish (*Protopterus annectens*) during lateral undulatory swimming. *J Exp Biol* 211:1612–1622.
36. Aleyev YG (1977) *Nekton* (Junk, The Hague).
37. Várkonyi PL, Kiemel T, Hoffman K, Cohen AH, Holmes P (2008) On the derivation and tuning of phase oscillator models for lamprey central pattern generators. *J Comput Neurosci* 25:245–261.
38. Grillner S, Williams T, Lagerbäck P-Å (1984) The edge cell, a possible intraspinal mechanoreceptor. *Science* 223:500–503.
39. Lim S, Peskin CS (2004) Simulations of the whirling instability by the immersed boundary method. *SIAM J Sci Comput* 25:2066–2083.